

Spectra, thresholds, and modal fields of a kite-shaped microcavity laser

Elena I. Smotrova,^{1,*} Victor Tsvirkun,² Iryna Gozhyk,² Clément Lafargue,² Christian Ulysse,³ Melanie Lebental,² and Alexander I. Nosich¹

¹Laboratory of Micro and Nano Optics, Institute of Radio-Physics and Electronics NASU, Kharkiv 61085, Ukraine

²Laboratoire de Photonique Quantique et Moleculaire, CNRS UMR 8537, Institut d'Alembert FR 3242, Ecole Nationale Supérieure de Cachan, Cachan 94235, France

³Laboratoire de Photonique et Nanostructures, CNRS UPR20, Route de Nozay, Marcoussis F-91460, France

*Corresponding author: elena.smotrova@gmail.com

Received March 7, 2013; accepted April 15, 2013;
posted April 30, 2013 (Doc. ID 186521); published May 30, 2013

We investigate the lasing spectra, threshold gain values, and emission directionalities for a two-dimensional microcavity laser with a “kite” contour. The cavity modes are considered accurately using the linear electromagnetic formalism of the lasing eigenvalue problem with exact boundary and radiation conditions. We develop a numerical algorithm based on the Muller boundary integral equations discretized using the Nystrom technique, which has theoretically justified and fast convergence. The influence of the deviation from the circular shape on the modal characteristics is studied numerically for the modes polarized in the cavity plane, demonstrating opportunities of directionality improvement together with preservation of a low threshold. These advantageous features are shown for the perturbed whispering-gallery modes of high-enough azimuth orders. Other modes can display improved directivities while suffering from drastically higher threshold levels. Experiments based on planar organic microcavity lasers confirm the coexistence of Fabry–Perot-like and whispering-gallery-like modes in kite-shaped cavities and show good agreement with the predicted far-field angular diagrams. © 2013 Optical Society of America

OCIS codes: (000.3860) Mathematical methods in physics; (000.4430) Numerical approximation and analysis; (140.3560) Lasers, ring; (140.3410) Laser resonators; (140.2050) Dye lasers.

<http://dx.doi.org/10.1364/JOSAB.30.001732>

1. INTRODUCTION

As already well documented, lasers with microcavities shaped as thin flat circular disks with smooth-enough rims can sustain whispering-gallery modes with very low thresholds [1–3]. The two-dimensional (2D) approximation, which implies replacement of the bulk refractive index by its effective value, works well for thinner-than-wavelength cavities. It predicts that the whispering-gallery mode thresholds are exponentially small relative to the in-plane optical size of the ideal circular cavity [4], although in practice they are restricted by the surface roughness. It is noteworthy that each mode with azimuth index $m > 0$ is double degenerate in a circular cavity. The emission on these modes is predominantly in the cavity plane, where it has low directivity because of as many as $2m$ identical beams [1–4]. However, applications often require sources of light with larger directivity of emission to process optical signals with higher efficiency and within a smaller volume.

A traditional method to obtain a narrow light beam is the use of a collimating lens with a low-directional source in its focus. The lens, however, is able to capture a portion of the light that is radiated in a limited angular sector. Besides, the use of a lens greatly increases the overall dimensions of a light-emitting device. If the lens is made smaller and placed nearer to a microlaser as suggested in [5], then the lens becomes a passive resonator optically coupled with the active resonator filled in with the gain medium and pumped.

This may lead, as has been shown in [6], to the pulling of the working-mode field into the lens and eventually to the unwanted growth of the lasing threshold.

As is evident, improvement of the directionality of mode emission requires a departure from the circular shape. Therefore, since the 1990s, researchers engaged in microlaser studies have been using the in-plane cavity shape as an engineering tool able to provide better directionality [7].

The later review papers [8–10] provide a reference source for these studies. Among the promising modified shapes, they have considered fully convex contours, such as ellipse, stadium, cut circle, various regular polygons, and others [11–15], and also partially concave “notched contours” [16,17]. Probably the highest expectations and the largest amount of effort have been associated with a spiral resonator, with an in-plane contour following an Archimedean spiral with a small step [18–22]. Still, the thresholds of lasing measured for such a shape are rather high and can be assigned to the discontinuous and strongly perturbing nature of a circular contour with a wavelength-sized step embedded therein. Therefore later efforts have been associated with a smoother shape provided by the limaçon curve [23–26]. Following similar considerations, it is possible to find other smooth perturbations of the circle. One of them is a curve called a “kite,” which we have selected for in-depth analysis. Unlike a limaçon, a kite is always smooth, although it can be both fully convex and partially concave depending on the perturbation parameter

(limaçon obtains an inflection point if the perturbation is above a certain value).

Still it is necessary to emphasize that simulations of micro-laser modes in [5,8,10–12,13,15–17,20,21,23–26] have been performed within the passive cavity model where instead of the actual threshold one looks for the mode-quality factors. As demonstrated in [27], low threshold is not equivalent to high Q factor although the former is inversely proportional to the latter—the overlap between the active region and the modal electric field is equally important. Therefore more adequate linear modeling of lasers is provided by the lasing eigenvalue problem (LEP) specifically tailored to consider open resonators equipped with active regions [4,6,9,22,27]. The LEP implies the introduction of material gain into the whole microcavity or at least an active region and enables extraction of the lasing frequencies and associated threshold values of material gain as eigenvalues.

The LEP approach can be implemented with the aid of any convergent numerical method originally developed for the analysis of passive cavities. A comparative review of such methods, from the “billiard theory” to finite-difference time-domain codes to integral equations, can be found elsewhere [9]. In this paper, we will use the Muller boundary integral equations (BIEs) [28,29] as reliable and efficient tools for analysis of the electromagnetic field in the presence of a 2D homogeneous dielectric object with an arbitrary smooth boundary. This is because other types of BIEs suffer from a serious drawback: they possess an infinite number of “spurious eigenvalues”—real numbers that are the eigenvalues of the interior electromagnetic problem where the boundary is assumed perfectly electrically conducting and the inside filling is assigned material parameters of the outer medium (e.g., free space) [30]. The spurious eigenvalues have no physical meaning and hinder the search for true complex eigenvalues with high Q factors. Examples of such IEs can be found in [5,12,17,20,21,23,25,26]; it should be added that these IEs can be still used in the search for low- Q eigenvalues.

In 2D, the Muller BIE is made in fact of two coupled equations. Besides being free of spurious eigenvalues, it is attractive because it is of the Fredholm second-kind type; i.e., it has smooth or integrable kernels. The Muller BIE can be discretized either with collocations [31] [i.e., meshing the boundary and introducing local basis functions; this is sometimes called the boundary-element method (BEM)] or with a Galerkin-type projection to global expansion functions [29]. As the optical cavities commonly have convex or at least star-like boundaries, the latter way of discretization leads to a more economic algorithm, although they both exhibit convergence by virtue of the Fredholm theorems. According to [29], the size of the resultant matrix is determined, in almost equal manner, by three quantities: the maximum optical size of the cavity, the normalized peak curvature of the boundary, and the desired accuracy in digits. This should be emphasized because, as a rule, the published works using BIE-BEM ignore the last two parameters and blindly rely on the “rule of thumb” of 10 mesh points per wavelength.

Here we build another efficient and convergent numerical algorithm for discretization of the Muller BIE, based on the interpolation polynomials and quadrature formulas as suggested in [32,33]. Some preliminary results of this analysis have been published in contributed conference papers

[34–36]; however, they are presented here in a more complete and convincing manner. Special attention is paid to the connection of the rate of convergence with the contour smoothness. The developed algorithm is applied to investigation of the H -polarized (vector \vec{E} in the cavity plane; sometimes called TE polarization) natural modes in 2D active kite-shaped resonators. As the kite contour sustains one symmetry axis, all modes split into two symmetry classes. We study the removal of the mode degeneracy in terms of the frequency and threshold due to the distortion of circular symmetry. The mode fields in the near and far zones are also studied in detail both for small and large deformations.

In the last section we present experimental data for the thin planar kite-shaped convex cavities and compare them with theoretically predicted results. The experiment has been made on the dye-doped polymer microlasers, and it confirmed the coexistence of several types of modes, notably the perturbed whispering-gallery modes and the quasi-Fabry–Perot modes.

2. LINEAR MODEL OF A MICROCAVITY LASER

A. Lasing Eigenvalue Problem

The geometry of a generic 2D open dielectric resonator with a smooth contour and the notations used are shown in Fig. 1. We denote the boundary of the resonator as Γ , the outer domain as D_e , and the inner domain as D_i . We assume that \vec{n} is the outer normal unit vector to the boundary Γ , and ν_j ($j = i, e$) are the refractive indices of the nonmagnetic resonator material and the outer space, respectively. Throughout this paper an $\exp(-i\omega t)$ factor is used implicitly to express time dependence.

For such a cavity subjected to uniform pumping, the LEP [4,27] implies that the inner domain is filled with a gain material so that the associated refractive index has a nonzero negative imaginary part, $\nu_i = \alpha_i - i\gamma$ ($\gamma > 0$). The outer space is assumed lossless, $\nu_e = \alpha_e$. Passive dielectric cavities ($\gamma \leq 0$) are known to possess an infinite number of discrete complex-valued natural frequencies or, equivalently, wavenumbers k_s (counted using an integer index s), each of which correspondingly generates a nonzero natural-mode electromagnetic field, $\{\vec{E}_s, \vec{H}_s\}$. It is the presence of the active region (here coinciding with the whole dielectric domain) that enables one to compensate for the radiation losses of any specific mode and

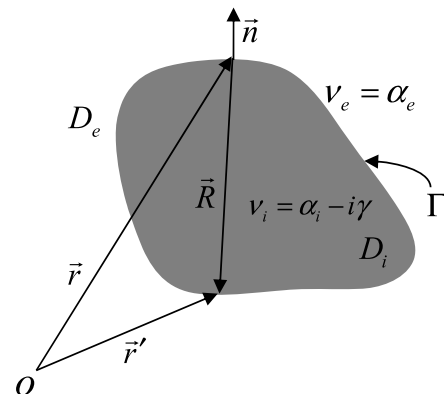


Fig. 1. Geometry of a uniformly active 2D dielectric resonator of arbitrary shape.

make its natural wavenumber k_s a real number. The associated value of $\gamma_s > 0$ is generally different for different modes and corresponds to the threshold gain in the resonator material. Note that the quantity of the modal gain coefficient per unit length used in the semiclassical theory of lasers with Fabry–Perot resonators is related to γ by $g = k\gamma$.

Mathematically, the problem of finding the values of k_s and γ_s and also the modal fields $\{\vec{E}_s, \vec{H}_s\}$ in the near and far zones can be seen as an electromagnetic eigenvalue problem (similar to the scattering problem but without the incident field). In view of the 2D cavity studied here, in order to characterize the electromagnetic field, it is sufficient to consider a scalar function U_j corresponding to the field components E_z or H_z , depending on the polarization, in the domains $D_j, j = i, e$. This function must be a solution to the boundary-value problem for the Helmholtz equations,

$$(\Delta + k_j^2)U_j(\vec{r}) = 0, \quad \vec{r} = (x, y) \in D_j, \quad (1)$$

with the boundary conditions on Γ ,

$$U_i(\vec{r}) = U_e(\vec{r}); \quad \eta_i \partial U_i(\vec{r}) / \partial n = \eta_e \partial U_e(\vec{r}) / \partial n, \quad (2)$$

and additional conditions of (i) local power finiteness and (ii) outgoing-wave behavior (Sommerfeld radiation condition) for U_e at infinity [4,27]. The coefficients in Eq. (1) are defined in such a way that $k_j = k\nu_j$. The boundary conditions (2) follow from the demand that the tangential field components are continuous across Γ . Therefore the constants in Eq. (2) are defined as follows: $\eta_j = 1/\nu_j^2$ in the case of H polarization and $\eta_j = 1$ for E polarization. The goal is to find the values of pairs of real numbers (k_s, γ_s) , which generate nonzero functions $U_j(\vec{r})$.

Note that a real value for k_s implies that the natural mode at the threshold of lasing does not attenuate in time and decays in space as a usual cylindrical wave, $O(r^{-1/2})$. Thus, the introduction of the active region characterized with the aid of $\gamma > 0$ leads to physically reasonable modal field behavior and opens direct access to the mode thresholds. The fact that the LEP is still a linear boundary-value problem should not be surprising because at threshold the field amplitude of any real laser is vanishingly small. More detailed discussion on the LEP and its connection to the optical theorem and the semiclassical theory of lasers can be found in [27].

B. Reduction to the Muller Boundary Integral Equations

For either of the two alternative polarizations, the reduction of the 2D electromagnetic-field eigenvalue problem to a BIE is based on the use of Green's formulas [28,32]. This can be done in many ways; however, only the Muller BIE possesses the full equivalency to the original boundary-value problem for Maxwell equations with all additional conditions, i.e., does not give artificial raise to spurious eigenvalues [30].

We first introduce Green's functions for the homogeneous media, $G_j(\vec{r}, \vec{r}')$, which are the solutions of the 2D Helmholtz equations with the Dirac delta function $\delta(\vec{r}, \vec{r}')$ at the right-hand side. For a homogeneous medium with a refractive index of ν_i , this is $G_j(\vec{r}, \vec{r}') = (i/4)H_0^{(1)}(k_j R)$, where $R = |\vec{r} - \vec{r}'|$ is the distance between the points \vec{r} and \vec{r}' , and $H_0^{(1)}(\cdot)$ is the Hankel function of the first kind and zero-order.

Then, applying the second Green's formula to the functions $G_j(\vec{r}, \vec{r}')$ and U_j , we obtain (see also [37])

$$U_j(\vec{r}) = \mp \int_{\Gamma} \left(U_j(\vec{r}') \frac{\partial G_j(\vec{r}, \vec{r}')}{\partial n'} - G_j(\vec{r}, \vec{r}') \frac{\partial U_j(\vec{r}')}{\partial n'} \right) dl', \quad \vec{r} \in D_j, \quad (3)$$

where dl' is the infinitesimal arc element on Γ .

Denote $\varphi(\vec{r}) = U_i(\vec{r})$ and $\psi(\vec{r}) = \partial U_i(\vec{r}) / \partial n$, $\vec{r} \in \Gamma$. Then from the boundary conditions (2) it follows that $U_e(\vec{r}) = \varphi(\vec{r})$ and $\partial U_e(\vec{r}) / \partial n = (\eta_i / \eta_e) \psi(\vec{r})$, $\vec{r} \in \Gamma$. Further, in Eq. (3), move the point \vec{r} to the contour Γ . Taking into account that the single-layer potential is continuous when crossing the boundary [32], we obtain

$$\varphi(\vec{r}) + \int_{\Gamma} \varphi(\vec{r}') A(\vec{r}, \vec{r}') dl' - \int_{\Gamma} \psi(\vec{r}') B(\vec{r}, \vec{r}') dl' = 0. \quad (4)$$

Kernels $A(\vec{r}, \vec{r}')$ and $B(\vec{r}, \vec{r}')$ are given below. On the differentiation of Eq. (3) in the normal \vec{n} and taking into account the properties of the normal derivatives of the single- and double-layer potentials [32], we obtain the second integral equation,

$$\frac{\eta_i + \eta_e}{2\eta_e} \psi(\vec{r}) + \int_{\Gamma} \varphi(\vec{r}') C(\vec{r}, \vec{r}') dl' - \int_{\Gamma} \psi(\vec{r}') D(\vec{r}, \vec{r}') dl' = 0. \quad (5)$$

The set of equations (4) and (5) forms the set of the Muller BIE. Here, the kernel functions are

$$A(\vec{r}, \vec{r}') = \partial G_i(\vec{r}, \vec{r}') / \partial n' - \partial G_e(\vec{r}, \vec{r}') / \partial n', \quad (6)$$

$$B(\vec{r}, \vec{r}') = G_i(\vec{r}, \vec{r}') - (\eta_i / \eta_e) G_e(\vec{r}, \vec{r}'), \quad (7)$$

$$C(\vec{r}, \vec{r}') = \partial^2 G_i(\vec{r}, \vec{r}') / \partial n \partial n' - \partial^2 G_e(\vec{r}, \vec{r}') / \partial n \partial n', \quad (8)$$

$$D(\vec{r}, \vec{r}') = \partial G_i(\vec{r}, \vec{r}') / \partial n - (\eta_i / \eta_e) \partial G_e(\vec{r}, \vec{r}') / \partial n. \quad (9)$$

The normal derivatives of the Green's functions are calculated after the following expressions:

$$\partial G_j(\vec{r}, \vec{r}') / \partial n' = (i/4) k_j H_1^{(1)}(k_j R) (\vec{R} \cdot \vec{n}') / R, \quad (10)$$

$$\partial G_j(\vec{r}, \vec{r}') / \partial n = (-i/4) k_j H_1^{(1)}(k_j R) (\vec{R} \cdot \vec{n}) / R, \quad (11)$$

$$\begin{aligned} \frac{\partial^2 G_j(\vec{r}, \vec{r}')}{\partial n \partial n'} = & -\frac{ik_j^2}{4} H_2^{(1)}(k_j R) \frac{(\vec{R} \cdot \vec{n}')(\vec{R} \cdot \vec{n})}{R^2} \\ & + \frac{ik_j}{4} H_1^{(1)}(k_j R) \frac{(\vec{n}' \cdot \vec{n})}{R}. \end{aligned} \quad (12)$$

In Eqs. (6)–(12), the quantities $(\vec{R} \cdot \vec{n})$, $(\vec{R} \cdot \vec{n}')$, and $(\vec{n}' \cdot \vec{n})$ are the scalar products of the corresponding vectors. Assume that the contour Γ parameterization is performed with the aid of the function $r(t) = \{x(t), y(t)\}$. Assuming that the variables t and τ in parametric form correspond to \vec{r} and \vec{r}' , the distance between two points on the contour is

$R = ([x(t) - x(\tau)]^2 + [y(t) - y(\tau)]^2)^{1/2}$, and the outer normal unit vector to the boundary is $\vec{n} = (1/L(t))(dy/dt; -dx/dt)$, where $L(t)$ is the Jacobian $L(t) = [(dx/dt)^2 + (dy/dt)^2]^{1/2}$.

C. Limiting Behavior of the Kernels

Thus, the kernels of the Muller BIE are linear combinations of either the Green’s functions of the homogeneous media having parameters of the outer and inner media, or their normal derivatives of the first and second-order. The kernel functions $A(t, \tau)$ in Eq. (6) and $D(t, \tau)$ in Eq. (9) are continuous at all points of a smooth contour at $t \rightarrow \tau$. This is conditioned by the following property (see, for instance, [38]):

$$\partial G_j(t, t) / \partial n = \chi_0(t) / 2, \tag{13}$$

where $\chi_0(t)$ is the curvature (see [39]) of the contour Γ at the point \vec{r} . The kernel functions $B(t, \tau)$ in Eq. (7) and $C(t, \tau)$ in Eq. (8) have logarithmic singularities. If $t \rightarrow \tau$, then the limiting behavior of these functions is given by the expressions

$$B(t, \tau) \underset{t \rightarrow \tau}{\cong} - (1/2\pi)[1 - \eta_i/\eta_e] \ln R, \tag{14}$$

$$C(t, \tau) \underset{t \rightarrow \tau}{\cong} - (1/2\pi)(k_i^2 - k_e^2) \ln R. \tag{15}$$

Note that the kernel $B(t, \tau)$ is singular only in the case of the H polarization; in the case of the E polarization, it is continuous. This analysis enables one to choose the appropriate method of discretization of the integral equations discussed in the next section.

D. Discretization Using the Quadratures

As mentioned, there are several approaches to a reasonable discretization of BIEs. One of the most efficient discretization techniques is the method of quadratures, also known as the Nystrom method [32,33,37,40,41]. This method is based on the approximation of smooth unknown functions by certain polynomials and the replacement of the integrals with approximate sums using the appropriate quadrature formulas. Therefore the main point in the development of corresponding numerical algorithms is placed on the derivation of quadrature formulas that correctly take into account the behavior of the integrand functions and, most importantly, their possible singularities.

In this paper, we will consider the discretization of integral equations with closed contours of integration that admit a regular analytical 2π -periodic parameterization with the aid of a function $r(t) = \{x(t), y(t)\}$, $t \in [0, 2\pi]$. As some of the kernel functions (6)–(9) have logarithmic singularities, it is convenient to represent them in such a way that these singularities are extracted; for uniformity, this decomposition is performed for the smooth kernels as well,

$$F(t, \tau) = F_1(t, \tau) \ln \left[4 \sin^2 \frac{t - \tau}{2} \right] + F_2(t, \tau), \tag{16}$$

$$F = A, B, C, D,$$

where $A_1(t, \tau)$, $B_1(t, \tau)$, $C_1(t, \tau)$ and $D_1(t, \tau)$ are the analytic functions defined as follows:

$$A_1(t, \tau) = (-1/4\pi)[k_i J_1(k_i R) - k_e J_1(k_e R)](\vec{R} \cdot \vec{n}') / R,$$

$$B_1(t, \tau) = (-1/4\pi)[J_0(k_i R) - (\eta_i/\eta_e)J_0(k_e R)],$$

$$C_1(t, \tau) = (1/4\pi)[k_i^2 J_2(k_i R) - k_e^2 J_2(k_e R)](\vec{R} \cdot \vec{n}')(\vec{R} \cdot \vec{n}) / R^2 - (1/4\pi)[k_i J_1(k_i R) - k_e J_1(k_e R)](\vec{n}' \cdot \vec{n}) / R,$$

$$D_1(t, \tau) = (1/4\pi)[k_i J_1(k_i R) - (\eta_i/\eta_e)k_e J_1(k_e R)](\vec{R} \cdot \vec{n}) / R. \tag{17}$$

The functions $A_2(t, \tau)$, $B_2(t, \tau)$, $C_2(t, \tau)$, $D_2(t, \tau)$ are found from Eq. (16) by taking into account Eqs. (6)–(9). Further, we introduce an equidistant mesh of nodes on the contour Γ at $t_p = \pi p / N$, $p = 0, 1, \dots, 2N - 1$. The integrals for each part of the kernels are replaced with the sums using the quadrature formulas. For the logarithmic parts, we use the quadrature formula derived through the approximation of the integrand functions by trigonometric polynomials [32,33,41],

$$\int_0^{2\pi} \ln \left[4 \sin^2 \frac{t - \tau}{2} \right] F_1(t, \tau) f(\tau) L(\tau) d\tau \approx \sum_{p=0}^{2N-1} P_p^{(N)}(t) F_1(t, t_p) f(t_p) L(t_p), \tag{18}$$

where the trigonometric polynomial of the order N has the form

$$P_p^{(N)}(t) = -(2\pi/N) \sum_{m=1}^{N-1} \cos[m(t - t_p)] / m - (\pi/N^2) \cos[N(t - t_p)]. \tag{19}$$

For the other, continuous parts of kernels we use the trapezoidal rule [42]

$$\int_0^{2\pi} F_2(t, \tau) f(\tau) L(\tau) d\tau \approx (\pi/N) \sum_{p=0}^{2N-1} F_2(t, t_p) f(t_p) L(t_p). \tag{20}$$

In expressions (18) and (20), it is implied that $F_1 = A_1, B_1, C_1, D_1$ and $F_2 = A_2, B_2, C_2, D_2$ and also $f = \varphi, \psi$. Upon replacement, in the integral equations (4) and (5), of the integrals by the quadratures (18) and (20), the following $4N \times 4N$ matrix equation is obtained:

$$[\mathbf{I} + \mathbf{A}] \begin{pmatrix} \Phi \\ \Psi \end{pmatrix} = 0, \tag{21}$$

where the vectors of unknowns are $\Phi = \{\varphi(t_p)\}_{p=0, 2N-1}$ and $\Psi = \{\psi(t_p)\}_{p=0, 2N-1}$, and the matrix \mathbf{A} has a block structure,

$$\mathbf{A} = \begin{bmatrix} A & -B \\ C & -D \end{bmatrix}. \tag{22}$$

Every block has the size of $2N \times 2N$, and its elements are given by

$$\begin{aligned}
A &= \{(P_p^{(N)}(t_s)A_1(t_s, t_p) + (\pi/N)A_2(t_s, t_p))L(t_p)\}_{p,s=0}^{2N-1}, \\
B &= \{2\eta_e/(\eta_e + \eta_i)(P_p^{(N)}(t_s)B_1(t_s, t_p) + (\pi/N)B_2(t_s, t_p))L(t_p)\}_{p,s=0}^{2N-1}, \\
C &= \{(P_p^{(N)}(t_s)C_1(t_s, t_p) + (\pi/N)C_2(t_s, t_p))L(t_p)\}_{p,s=0}^{2N-1}, \\
D &= \{2\eta_e/(\eta_e + \eta_i)(P_p^{(N)}(t_s)D_1(t_s, t_p) + (\pi/N)D_2(t_s, t_p))L(t_p)\}_{p,s=0}^{2N-1}.
\end{aligned} \tag{23}$$

It is convenient to introduce a dimensionless value of $\kappa = ka$, where a is some characteristic dimension of the 2D cavity. Then, the lasing eigenvalues (κ, γ) are the roots of a determinantal equation,

$$\det[\mathbf{I} + \mathbf{A}(\kappa, \gamma)] = 0. \tag{24}$$

Considering the accuracy of computations, we can note that if the integrand function is analytic and 2π periodic, then, according to [32], the error associated with Eqs. (18) and (20) is of the order of $O[\exp(-\sigma N)]$, where $2N$ is the number of nodes in the quadrature and σ is the half-width of the strip in the complex plane to which the integrand functions $F_{1,2}(t, \tau)f(\tau)L(\tau)$ can be holomorphically continued.

The roots (κ_s, γ_s) of the approximate determinantal equation are found numerically using the iterative-type secant method. In the process of our computations, the accuracy of determining the roots has been fixed at the level of 10^{-7} . The number of iterations strongly depends on the nearness of the initial guess to the true eigenvalue.

3. MODES OF MICROCAVITY LASER WITH KITE CONTOUR

In this section, we present a numerical study of the H -polarized lasing modes of a 2D uniformly active cavity shaped as a kite. Here, we can consider the cavity contour as a deformed circle and therefore study, in fact, the effect of the perturbation of the circle on the spectrum of lasing frequencies and associated thresholds, as well as on the directionality of the emission. As a kite-contour parameterization, we use 2π -periodic analytic functions

$$x(t) = a(\cos t + \delta \cos 2t - \delta), y(t) = a \sin t, \tag{25}$$

where a is the radius of a circular cavity in the limiting case where $\delta = 0$; we will study in detail the cases of a fully convex contour for $\delta = 0.165$ and a partially concave contour for $\delta = 0.5$. As explained in the previous section, the LEP eigenvalues, i.e., the normalized lasing frequencies κ_s and the associated thresholds γ_s , are the roots of the determinantal equation (24) of the order N . We solve this equation using the iterative Newton method, which requires initial-guess values of the roots. These values can be found by visualizing the reliefs of the absolute value of the determinant as a function of two parameters, κ and γ , in a selected range of their variation.

In Figs. 2(a) and 2(b), we show two examples of such reliefs for $\delta = 0.165$ (fully convex contour) and $\delta = 0.5$ (partially concave contour) in the range of normalized frequencies ka between 8.0 and 10.0 that corresponds to the medium-sized cavity. The vertical axis corresponds to γ in logarithmic scale to distinguish between the modes having close thresholds.

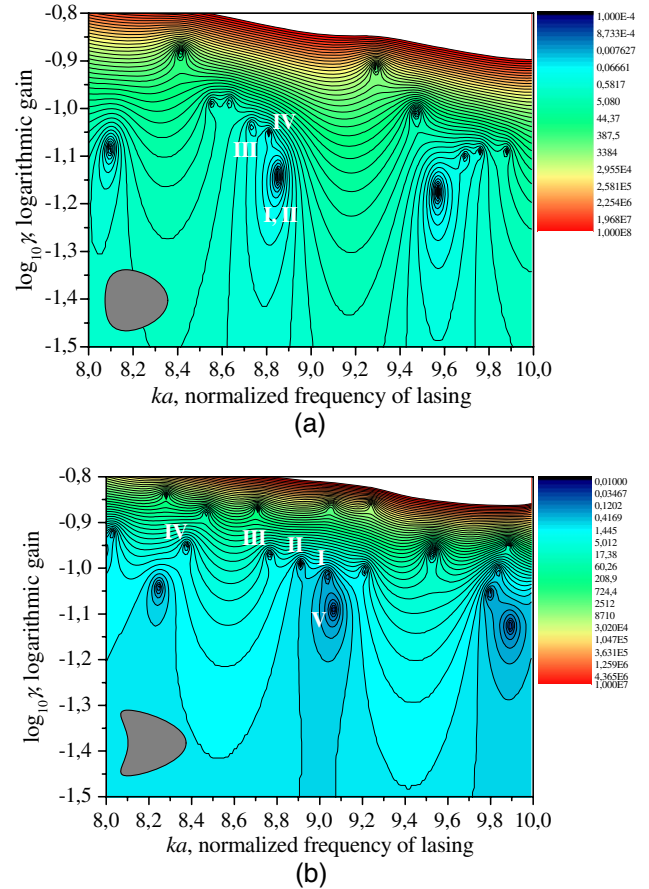


Fig. 2. Relief of determinant (a) for a fully convex kite $\delta = 0.165$ and (b) for a partially concave $\delta = 0.5$. Other parameters are $\alpha = 1.5$ and $N = 50$. Marks correspond to the field patterns in Figs. 4 and 5.

The minima on the reliefs indicate the locations of eigenvalues. As one can see, the plane (κ, γ) is inhabited by the modes of the kite (i.e., by the LEP solutions) in somewhat different ways for a fully convex and a partially concave shape. In the former case ($\delta = 0.165$), there is a sequence of three minima in the shown range that correspond to modes with noticeably lower thresholds than all other modes. As will be further demonstrated, each of these minima hides a close doublet of two whispering-gallery-like (WG-like) modes of different parities across the x axis, while the other modes, with higher thresholds, are the Fabry–Perot-like (FP-like) and “volume” modes. Here, the FP-like modes are actually a subset of the volume modes displaying a chain of field maxima along a certain, generally curved, line inside the kite. In the latter case ($\delta = 0.5$), there are also three minima seen below the others in terms of γ ; however, each of them contains only one mode that keeps certain WG-like features (see below) and has an x -odd magnetic field. A corresponding x -even sister mode has been already perturbed so much that its threshold is comparable or even larger than for the non-WG-like modes.

In Figs. 3(a) and 3(b), we present the dynamics of the lasing frequencies and thresholds in the kite laser with varying deformation. Here, the curves for two pairs of modes are presented. One of them originates from two degenerate at $\delta = 0$ dipole modes of the $H_{1,4}$ type that have no WG behavior. The other is related to two degenerate at $\delta = 0$ modes of the $H_{10,1}$ type that are clearly WG modes—to emphasize this, we will

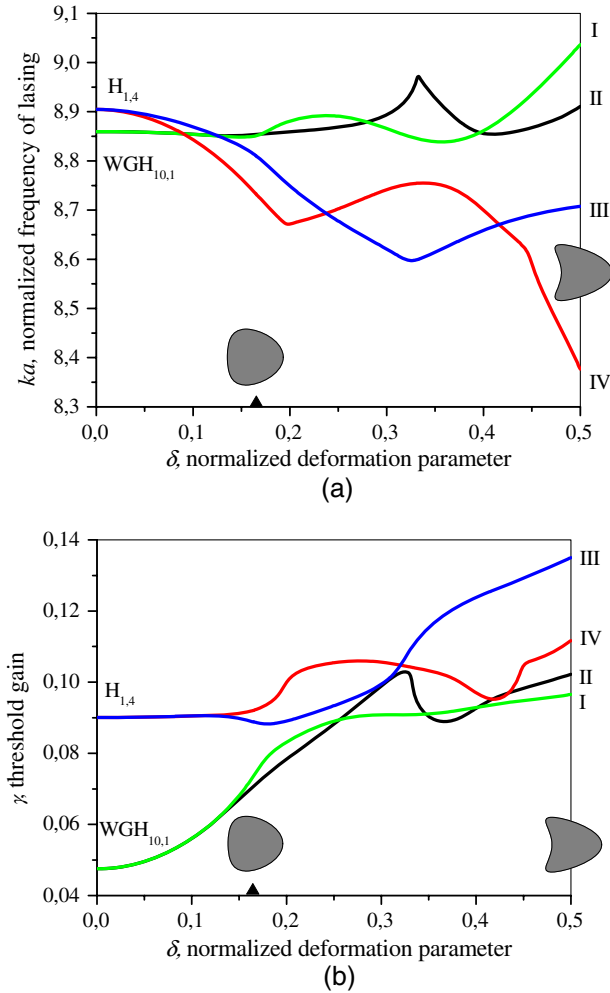


Fig. 3. (a) Lasing frequencies and (b) thresholds as functions of the kite deformation parameter δ , for the doublet of quasi- $WGH_{10,1}$ (green and black lines) and quasi- $H_{1,4}$ (blue and red) modes, $\alpha = 1.5, N = 50$. Marks I-IV correspond to similar marks in Figs. 2, 4, and 5.

denote them as quasi- $WGH_{10,1}$. So far, as the deformation is small, at least if $\delta < 0.15$, all four modes display similar behavior, and actually WG-like modes are nearly degenerate while non-WG modes become essentially split only in terms of frequency. More dramatic changes occur if δ is getting larger and especially around and after the critical value of 0.251 beyond which the kite exhibits a concave part on its boundary. Each mode keeps field parity across the x axis; however, its pattern varies considerably. Note that the theorems of operator-valued function analysis guarantee that each $k_s(\delta)$ and $\gamma_s(\delta)$ are continuous functions of the argument. We label the corresponding continuous modal branches as I, II, III, and IV.

Figures 4 and 5 demonstrate the amplitude near-field and far-field patterns for the doublets of modes $H_{1,4}$ and $WGH_{10,1}$ in a weakly deformed convex kite-shaped microlaser and their eventual counterparts for the large deformation, respectively. Labels I-IV (V) correspond to marks in Figs. 2(a) and 2(b), and also Figs. 3(a) and 3(b). These field patterns enable one to see how the progressive deformation turns some of the initially WG-like modes into FP-like and volume modes. In addition, the field patterns of mode V in Fig. 5 demonstrate that in a strongly deformed kite cavity, a specific family of modes

appears that adapt themselves to the appearance of a concave part of the boundary. We have called them “horseshoe-like” (HS-like) modes; they can be viewed, on the one hand, as partial WG-like modes standing along the part of the cavity boundary that is still concave and, on the other hand, as specific FP-like modes standing along the curved path between the two most curved parts of the same boundary.

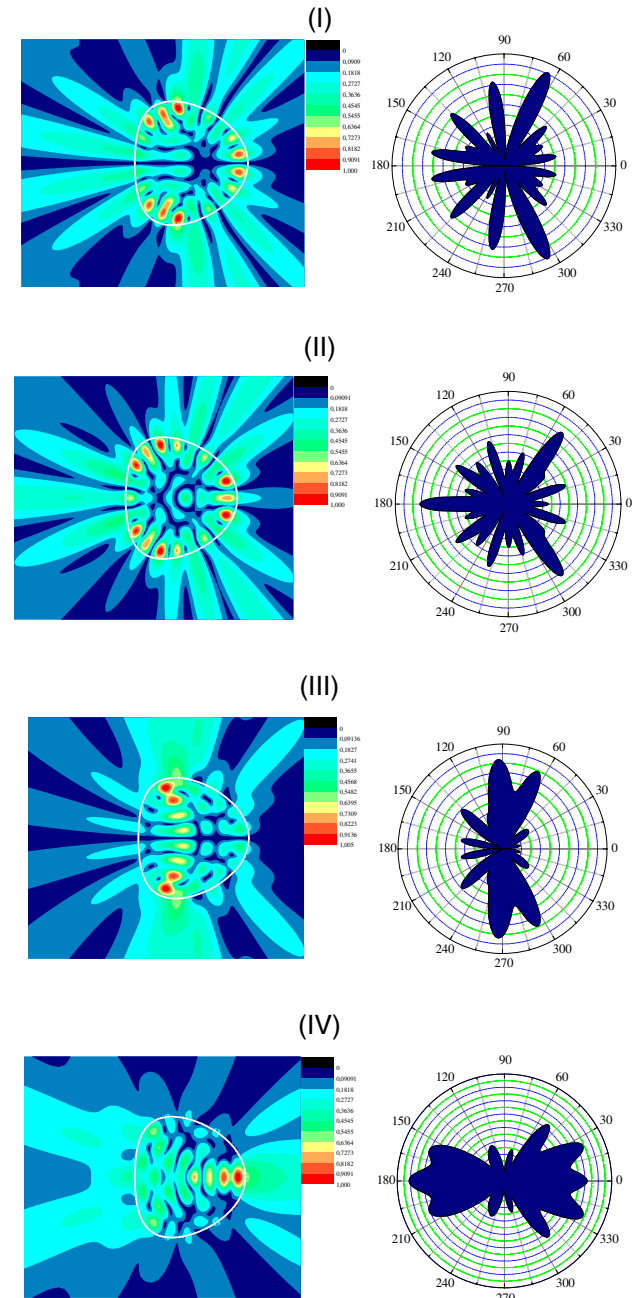


Fig. 4. Near- and far-field patterns of $|H_z|$ for two modes that form the quasi- $WGH_{10,1}$ doublet (I), (II) and quasi- $H_{1,4}$ doublet (III), (IV) in a kite with contour parameter $\delta = 0.165$. These field patterns correspond to the marks in Figs. 2 and 3. Mode (I) is an odd WG-like one with $\kappa = 8.8511, \gamma = 7.352 \cdot 10^{-2}$, and $D = 3.86$. Mode (II) is an even WG-like one with $\kappa = 8.8534, \gamma = 7.076 \cdot 10^{-2}$, and $D = 3.33$. Mode (III) is an odd FP-like one with $\kappa = 8.8105, \gamma = 8.884 \cdot 10^{-2}$, and $D = 3.54$. Mode (IV) is an even FP-like one with $\kappa = 8.733, \gamma = 9.207 \cdot 10^{-2}$, and $D = 2.8$. Other parameters are $\alpha = 1.5$ and $N = 50$.

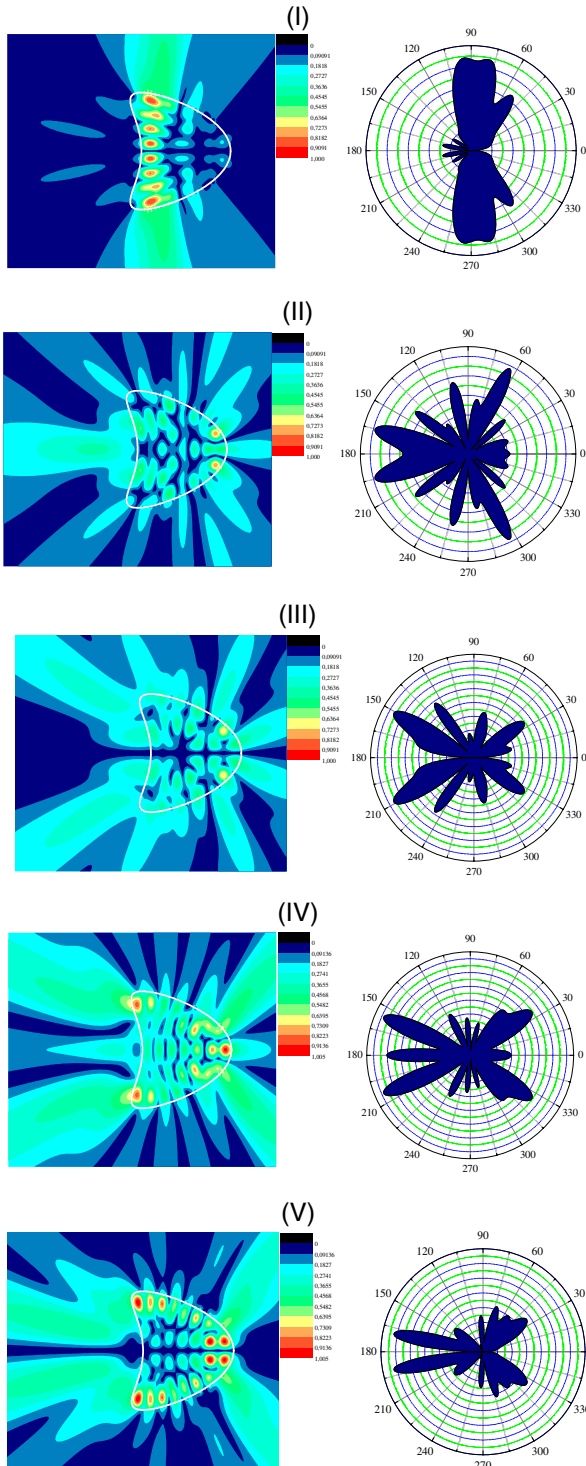


Fig. 5. Same as in Fig. 4 in a kite with contour parameter $\delta = 0.5$. These field patterns correspond to marks in Figs. 2 and 3. Mode (I) is an odd FP-like one with $\kappa = 9.0367$, $\gamma = 9.655 \times 10^{-2}$, and $D = 3.49$. Mode (II) is an even FP-like one with $\kappa = 8.9111$, $\gamma = 0.1022$, and $D = 3.23$. Mode (III) is an odd volume one with $\kappa = 8.7076$, $\gamma = 0.135$, and $D = 4.08$. Mode (IV) is an even volume one with $\kappa = 8.3764$, $\gamma = 0.1117$, and $D = 3.95$. Mode (V) is an odd HS-like one with $\kappa = 9.0652$, $\gamma = 8.1136 \times 10^{-2}$, and $D = 5.65$. Other parameters are $\alpha = 1.5$ and $N = 50$.

HS-like modes also have rather low thresholds and radiate predominantly into the half-space toward which the concave part of the contour is oriented.

A far-field expression for the mode field can be obtained using the integral (3) and the asymptotic of the Hankel function for large arguments [42], leading to the following expression:

$$U_e(r, \theta) \underset{r \rightarrow \infty}{=} -(i + 1)e^{ik_e r} \Phi(\theta) / (4\sqrt{\pi k_e r}), \quad (26)$$

where θ is the angle of observation and $\Phi(\theta)$ is the far-field angular pattern,

$$\Phi(\theta) = \int_{\Gamma} \{i\varphi k_e [\vec{n}' \cdot (\cos \theta, \sin \theta)] + (\eta_i / \eta_e) \psi\} e^{-ik_e i \vec{r}' \cdot (\cos \theta, \sin \theta)} d\vec{l}'. \quad (27)$$

The directionality of mode emission can be conveniently characterized using the quantity borrowed from the antenna theory and referred to as directivity,

$$D = (2\pi/P)|\Phi(\theta_{\max})|^2, \quad P = \int_0^{2\pi} |\Phi(\theta)|^2 d\theta, \quad (28)$$

where θ_{\max} is the angle of the main beam radiation in the half-space $0 \leq \theta \leq \pi$ and P is, within a constant, the total power radiated by a lasing mode. The values of directivity associated with each mode are also indicated in Figs. 4 and 5. Note that all modes of a circular resonator with azimuth index $m > 1$ and far-field patterns $\Phi(\theta) = \cos(m\theta)$ or $\sin(m\theta)$ have $D = 2$ and that omnidirectional emission for $m = 0$ results in $D = 1$. Note also that an x -odd mode cannot have less than two main beams and thus it displays generally (although not always) smaller values of directivity than its sister mode of the x -even parity. As is visible, the directivity of any mode of the kite cavity is larger than for the unperturbed WG mode of the circle.

In Figs. 6(a) and 6(b), we present, respectively, the reliefs of the absolute value of determinant on the plane (k, γ) in the range of normalized frequencies ka from 20 to 24 that correspond to relatively large-sized cavities and its zoomed part corresponding to the area shown by dashed lines, for a kite with a small deformation ($\delta = 0.165$). We do not show the reliefs for the larger deformations because, as is already clear from the above presented data, in that case no low-threshold modes are expected.

In Fig. 6(a), one can see a familiar almost periodic sequence of minima in the domain of low thresholds around 0.01—these are the closely spaced doublets of the WG-like modes surviving under small deformation. The zoomed relief in Fig. 6(b) reveals a dense collection of non-WG modes having thresholds between 0.05 and 0.035. The patterns presented in Fig. 7 demonstrate examples of the near and far fields of some of these modes, with the values of normalized frequencies, material thresholds, and directivities of emission explained in the caption. Note that to keep the accuracy at the same level as for the data presented in Figs. 2–5, we had to take twice larger values of N in the interpolation scheme in our numerical algorithm.

A somewhat counterintuitive result is that the quasi-WG modes whose inner fields are compressed to the resonator boundary have larger values of directivity than the FP-like and other non-WG-like modes. The domains of the intensive scattering are the parts of the kite contour that have larger

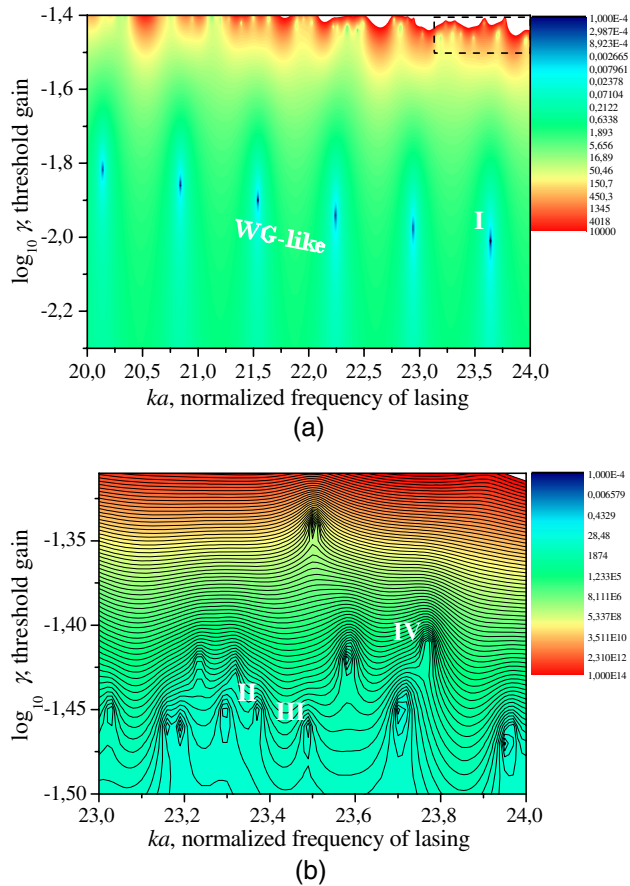


Fig. 6. Relief of determinant (a) for the fully convex kite $\delta = 0.165$ and (b) for a zoomed domain shown with dashed lines. Other parameters are $\alpha = 1.5$ and $N = 100$. Marks correspond to the field patterns in Fig. 7.

curvatures, and the sector of radiation of several of the most intensive beams can be explained using the ray-tracing and tunneling considerations as shown [15,17,23–26]. If one takes into account that the WG-like modes have considerably lower thresholds than other modes, one can state that these modes form a remarkable subset within the ensemble of solutions for the fully convex kite cavity. This is true as far as the whole cavity is uniformly active. If pumping is performed selectively using a focused beam or shaped electrodes, then the overlap between the active region and modal electric field becomes important [27].

4. COMPARISON WITH EXPERIMENTAL DATA

Experiments have been performed on kite-shaped dye-doped polymer microlasers. Planar dimensions of such microlasers (~ 100 – $200 \mu\text{m}$) are several orders of magnitude larger than both the cavity thickness (~ 0.5 – $0.8 \mu\text{m}$) and the emission wavelength ($\sim 0.6 \mu\text{m}$), allowing us to consider these cavities as quasi-2D components. The fabrication work flow consists of two steps. First the dye-doped polymer layer is obtained by spin coating a mixture of poly(methylmetacrylate) (Microchem 495 PMMA A6) polymer with 5 wt. % of a high-purity noncommercial dye MD7 (4,4-difluoro-8-mesityl-3,5-di(naphthalen-1-yl)-4-bora-3a,4a-diaza-s-indacene) [43] on a commercial $\text{SiO}_2(2 \mu\text{m})/\text{Si}$ substrate. The kite contour is then

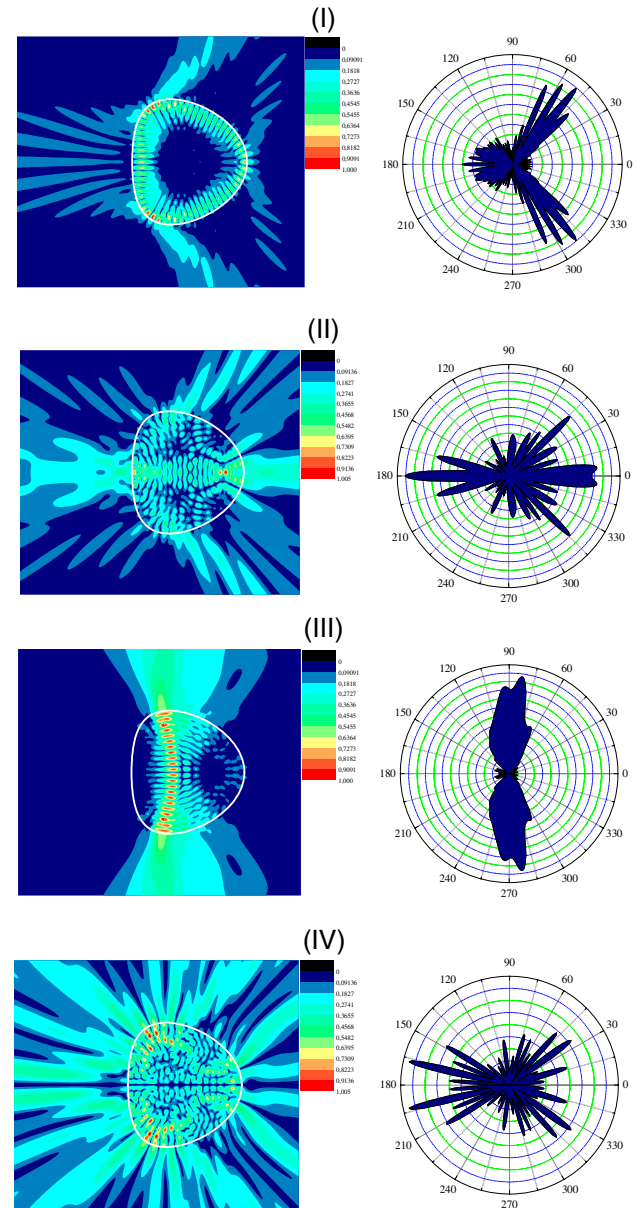


Fig. 7. Near- and far-field patterns of $|Hz|$ for the WG-like, FP-like, and volume modes. These field patterns correspond to the marks in Fig. 6. Mode (I) is an even WG-like one with $\kappa = 23.6404$, $\gamma = 9.7644 \times 10^{-3}$, and $D = 6.78$. Mode (II) is an even FP-like one with $\kappa = 23.3738$, $\gamma = 3.5438 \times 10^{-2}$, and $D = 5.48$. Mode (III) is an odd FP-like one with $\kappa = 23.4871$, $\gamma = 3.4565 \times 10^{-2}$, and $D = 5.73$. Mode (IV) is an odd volume one with $\kappa = 23.7649$, $\gamma = 3.8783 \times 10^{-2}$, and $D = 6.7$. Other parameters are $\alpha = 1.5$, $\delta = 0.165$, and $N = 100$.

obtained in the doped PMMA layer by means of electron-beam lithography (Vistec EBPG 5000+). This allows us to achieve an almost defect-free cavity surface with flat sidewalls.

During the experiment, a single microlaser is uniformly pumped from the top with a frequency-doubled pulsed Nd:YVO₄ laser (532 nm, 500 ps, 10 Hz). The microlaser emission is then collected in the lateral directions (within the cavity plane) with a lens (collection angle $\sim 6^\circ$), which focuses the emission into an optical fiber connected to a spectrometer (Acton SpectraPro 2500i) equipped with a cooled CCD camera (Princeton Instruments PIXIS 100) [44]. All experiments have been carried out at room atmosphere and temperature.

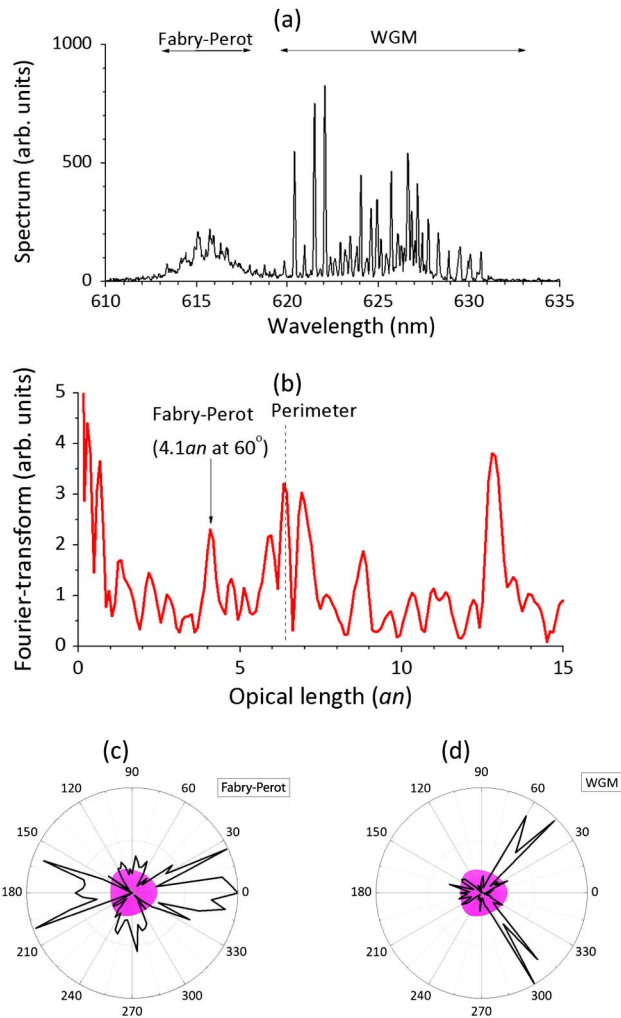


Fig. 8. Experimental emission characteristics of a microlaser with $a = 70 \mu\text{m}$ and $\delta = 0.165$. (a) Spectrum recorded in the direction 60° . (b) Fourier transform of the spectrum in (a). The horizontal axis is labeled in units of an , which is the optical length of the corresponding circle radius. (c), (d) Emission patterns for FP-like mode and WG-mode (WGM), respectively.

The experimental spectrum in Fig. 8(a) proves the coexistence of different modes, which can be identified through their different optical lengths in the Fourier transform of the spectrum [see Fig. 8(b)]. The explanation of the data processing is detailed in [44]. Some spectral peaks are then assigned to FP-like modes due to good agreement with the predicted optical length. The other peaks should correspond to quasi-WG modes, since their optical length is close to the perimeter. Moreover the identification of these two types of modes is reinforced by the analysis of the polarization states of their emission [45]. Actually, the FP-like mode was shown to be polarized mainly within the cavity plane, while WG-like modes exhibited prevalence for a polarization orthogonal to the cavity plane. These experiments confirm numerical prediction of the coexistence of FP-like and WG-like modes.

The angular far-field emission pattern of a given microlaser is recorded by rotating the cavity in its plane, the whole setup remaining unmodified. The plots in Figs. 8(c) and 8(d) correspond to the maximum peak over the pixels of a certain spectral region [610–619 nm for Fabry–Perot and 620–632 nm for

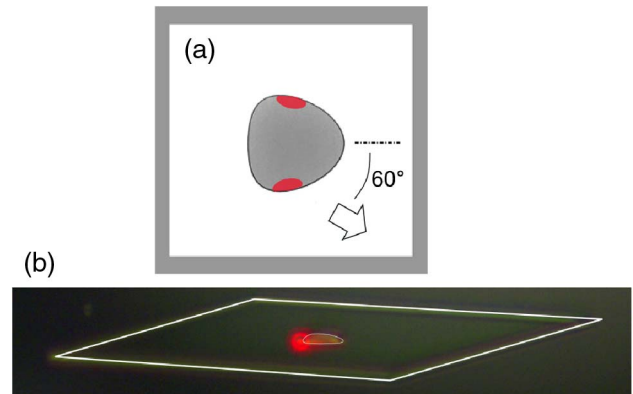


Fig. 9. Slightly oblique observation of light emission from a kite-shaped microlaser. (a) Scheme of the in-plane configuration. (b) Experimental image in real colors during lasing. The boundaries of the cavity and the layer-free part are emphasized with white lines.

WGM; see Fig. 8(a)] for each direction of observation. There is good qualitative agreement with the numerical predictions in Fig. 7, for instance between patterns Fig. 8(c) and Fig. 7(II), and between patterns Fig. 8(d) and Fig. 7(I).

In order to evidence the parts of the cavity boundary that are involved in the emission process, we examined the light outcoupling from the kite microlaser with the help of a CCD camera mounted on a teleobjective (Navitar 1-6232, zoom 6000). This setup is positioned almost in the cavity plane, in the direction of maximum emission of the quasi-WG modes [$\sim 60^\circ$; see Fig. 9(a)]. It is then possible to compare the location of the cavity under white light with the hot spots under pumping, as visible in Fig. 9(b). As depicted in Fig. 9(a), the light outcoupling regions seem then to be the points of the boundary with the highest curvature. This far-field observation is then consistent with the near-field pattern predicted by numerical simulations in Fig. 7(I).

The experiments (spectrum, far-field patterns, and imaging) are then in good agreement with the numerical predictions, in spite of a difference in ka of two orders of magnitude (~ 20 for simulations and 1000 for experiments).

Inferring the threshold values of different modes is the main advantage of the method presented in this article for analysis of dielectric cavities. At the current stage of study we do not exploit this advantage, as the primary goal of the experimental verification was to confirm the mode coexistence and directional emission properties. Still, based on experimental study, we can qualitatively confirm the predictions of the model, stating that the Fabry–Perot-like modes have higher thresholds compared to the WG-like modes. Proper study of this issue demands analysis of the influence of cavity size on thresholds of both modes types, and is left for the future studies.

5. CONCLUSIONS

We have considered a 2D model of the uniformly active dielectric open resonator with a smooth contour. As an instrument of analysis, we have used the Muller BIE adapted to extraction of the lasing spectra and thresholds via the LEP formulation. We have also presented the interpolation-type Nystrom method of the BIE reduction to the determinantal equation that has theoretically proven convergence. Implementing the developed algorithm, we have performed a systematic

numerical analysis of the lasing frequencies and thresholds, and also of the near- and far-zone fields for the modes of the resonator that is shaped as a kite with a deformation parameter, changing the smooth contour from fully convex to partially concave.

In the kite resonator, deformation of the contour from the circle leads to removal of the mode degeneracy and the appearance of doublets. The kite-cavity modes that are the perturbations of the WG modes whose fields are confined at the rim of the resonator are perturbed by the deformation in such a way that the thresholds of both modes in a doublet monotonically grow up if the parameter δ gets larger. However, in a fully convex kite, these modes are the most promising candidates for the working lasers because of the lucky combination of both the best thresholds and the best directionalities. Note that although their emission occurs predominantly onto one half-space, it is never “unidirectional” in the sense that it always has several main beams.

Comparison of the measured spectral compositions of kite-shaped microlasers and their far-field patterns with the computed spectra and patterns has enabled us to clearly identify the FP-like and WG-like modes in both cases. The measured emission patterns and the computed ones show good qualitative agreement, both in the direction of the most intensive radiation and in the “shining” parts of the cavity contour. The measured values of the lasing thresholds have displayed the expected difference between WG-like modes and FP-like modes, the latter being considerably higher than the former. More details on the threshold investigation will be presented in a separate publication.

Although 2D modeling describes the near and far fields in the cavity plane relatively well, sometimes a full 3D far field is needed. It can be found using either the near-to-far field transformation or the method of effective currents. Still the high- Q modes are known to radiate predominantly in the cavity plane [46].

ACKNOWLEDGMENTS

The authors thank J. Zyss and S. Bittner for encouragement and fruitful discussions, and G. Clavier, R. Méallet-Renault, and M. Dvorko from the PPSM laboratory at ENS de Cachan for providing the MD7 dye. This work was supported, in part, by the National Academy of Sciences of Ukraine via the State Target Program “Nanotechnologies and Nanomaterials” (project no. 1.1.3.45), the Ministry of European and Foreign Affairs of France, jointly with the State Agency for Science of Ukraine, via the Program “Dnipro,” and the European Science Foundation via the exchange grant of the Research Networking Programme “Newfocus” (for the first author) (no. 3823).

REFERENCES

- S. L. McCall, A. F. J. Levi, R. E. Slusher, S. J. Pearton, and R. A. Logan, “Whispering-gallery mode microdisk lasers,” *Appl. Phys. Lett.* **60**, 289–291 (1992).
- A. B. Matsko and V. S. Ilchenko, “Optical resonators with whispering-gallery modes-part I: basics,” *IEEE J. Sel. Top. Quantum Electron.* **12**, 3–14 (2006).
- A. B. Matsko and V. S. Ilchenko, “Optical resonators with whispering-gallery modes-part II: applications,” *IEEE J. Sel. Top. Quantum Electron.* **12**, 15–32 (2006).
- E. I. Smotrova, A. I. Nosich, T. Benson, and P. Sewell, “Cold-cavity thresholds of microdisks with uniform and non-uniform gain: quasi-3D modeling with accurate 2D analysis,” *IEEE J. Sel. Top. Quantum Electron.* **11**, 1135–1142 (2005).
- J.-W. Ryu and M. Hentschel, “Designing coupled microcavity lasers for high- Q modes with unidirectional light emission,” *Opt. Lett.* **36**, 1116–1118 (2011).
- E. I. Smotrova, J. Ctyroky, T. M. Benson, P. Sewell, and A. I. Nosich, “Lasing frequencies and thresholds of the dipole-type supermodes in an active microdisk concentrically coupled with a passive microring,” *J. Opt. Soc. Am. A* **25**, 2884–2892 (2008).
- A. F. J. Levi, R. E. Slusher, S. L. McCall, J. L. Glass, S. J. Pearton, and R. A. Logan, “Directional light coupling from microdisk lasers,” *Appl. Phys. Lett.* **62**, 561–563 (1993).
- H. G. L. Schwefel, H. E. Tureci, A. D. Stone, and R. K. Chang, “Progress in asymmetric resonant cavities: using shape as a design parameter in dielectric microcavity lasers,” in *Optical Microcavities*, K. Vahala, ed. (World Scientific, 2004), pp. 415–496.
- A. I. Nosich, E. I. Smotrova, S. V. Boriskina, T. M. Benson, and P. Sewell, “Trends in microdisk laser research and linear optical modeling,” *Opt. Quantum Electron.* **39**, 1253–1272 (2007).
- T. Harayama and S. Shinohara, “Two-dimensional microcavity lasers,” *Laser Photon. Rev.* **5**, 247–281 (2011).
- H. G. L. Schwefel, N. B. Rex, H. E. Tureci, R. K. Chang, and A. D. Stone, “Dramatic shape sensitivity of directional emission patterns from similarly deformed cylindrical polymer lasers,” *J. Opt. Soc. Am. B* **21**, 923–934 (2004).
- J. Wiersig, “Hexagonal dielectric resonators and microcrystal lasers,” *Phys. Rev. A* **67**, 023807 (2003).
- S.-K. Kim, S.-H. Kim, G.-H. Kim, H.-G. Park, D.-J. Shin, and Y.-H. Lee, “Highly directional emission from few-micron-size elliptical microdisks,” *Appl. Phys. Lett.* **84**, 861–863 (2004).
- C.-M. Lai, H.-M. Wu, P.-C. Huang, S.-L. Wang, and L.-H. Peng, “Single mode stimulated emission from prismlike gallium nitride submicron cavity,” *Appl. Phys. Lett.* **90**, 1106–1108 (2007).
- S. R. Dubertrand, E. Bogomolny, N. Djellali, M. Leblental, and C. Schmit, “Circular dielectric cavity and its deformations,” *Phys. Rev. A* **77**, 013804 (2008).
- S. V. Boriskina, T. M. Benson, P. Sewell, and A. I. Nosich, “ Q -factor and emission pattern control of the whispering gallery modes in notched microdisk resonators,” *IEEE J. Sel. Top. Quantum Electron.* **12**, 66–70 (2006).
- Q. J. Wang, C. Yan, N. Yu, J. Unterhinninghofen, J. Wiersig, C. Pflügl, L. Diehl, T. Edamura, M. Yamanishi, H. Kan, and F. Capasso, “Whispering-gallery mode resonators for highly unidirectional laser action,” *Proc. Natl. Acad. Sci. USA* **107**, 22407–22412 (2010).
- F. Courvoisier, V. Boutou, J. P. Wolf, R. K. Chang, and J. Zyss, “Deciphering output coupling mechanisms in spiral microcavities with femtosecond light bullets,” *Opt. Lett.* **30**, 738–740 (2005).
- T. Ben-Massaoud and J. Zyss, “Unidirectional laser emission from polymer-based spiral microdisks,” *Appl. Phys. Lett.* **86**, 241110 (2005).
- J. Wiersig and M. Hentschel, “Asymmetric scattering and nonorthogonal mode patterns in optical microspirals,” *Phys. Rev. A* **73**, 031802 (2006).
- M. Hentschel, T.-Y. Kwon, M. A. Belkin, R. Audet, and F. Capasso, “Angular emission characteristics of quantum cascade spiral microlasers,” *Opt. Express* **17**, 10335–10343 (2009).
- E. I. Smotrova, T. M. Benson, J. Ctyroky, R. Sauleau, and A. I. Nosich, “Optical fields of the lowest modes in a uniformly active thin sub-wavelength spiral microcavity,” *Opt. Lett.* **34**, 3773–3775 (2009).
- J. Wiersig and M. Hentschel, “Combining directional light output and ultralow loss in deformed microdisks,” *Phys. Rev. Lett.* **100**, 033901 (2008).
- Q. Song, W. Fang, B. Liu, S.-T. Ho, G. S. Solomon, and H. Cao, “Chaotic microcavity laser with high quality factor and unidirectional output,” *Phys. Rev. A* **80**, 041807 (2009).
- Q. H. Song, L. Ge, A. D. Stone, H. Cao, J. Wiersig, J.-B. Shin, J. Unterhinninghofen, W. Fang, and G. S. Solomon, “Directional laser emission from a wavelength-scale chaotic microcavity,” *Phys. Rev. Lett.* **105**, 103902 (2010).

26. Q. H. Song, L. Ge, J. Wiersig, J.-B. Shim, J. Unterhinninghofen, A. Eberspacher, W. Fang, G. S. Solomon, and H. Cao, "Wavelength-scale deformed microdisk lasers," *Phys. Rev. A* **84**, 063843 (2011).
27. E. I. Smotrova, V. O. Byelobrov, T. M. Benson, J. Ctyroky, R. Sauleau, and A. I. Nosich, "Optical theorem helps understand thresholds of lasing in microcavities with active regions," *IEEE J. Quantum Electron.* **47**, 20–30 (2011).
28. C. Muller, *Foundations of the Mathematical Theory of Electromagnetic Waves* (Springer, 1969).
29. S. V. Boriskina, T. M. Benson, P. Sewell, and A. I. Nosich, "Accurate simulation of 2-D optical microcavities with uniquely solvable boundary integral equations and trigonometric-Galerkin discretization," *J. Opt. Soc. Am. A* **21**, 393–402 (2004).
30. A. F. Peterson, "The 'interior resonance' problem associated with surface integral equations of electromagnetics: numerical consequences and a survey of remedies," *Electromagnetics* **10**, 293–312 (1990).
31. V. Rokhlin, "Rapid solution of integral equations of scattering theory in two dimensions," *J. Comput. Phys.* **86**, 414–439 (1990).
32. D. Colton and R. Kress, *Inverse Acoustic and Electromagnetic Scattering Theory* (Springer, 1998).
33. L. Wang, J. A. Cox, and A. Friedman, "Modal analysis of homogeneous optical waveguides by the boundary integral formulation and Nystrom method," *J. Opt. Soc. Am. A* **15**, 92–100 (1998).
34. E. I. Smotrova and A. I. Nosich, "Simulation of lasing modes in a kite-shaped microcavity laser," in *Proceedings of International Conference on Advanced Optoelectronics and Lasers* (IEEE, 2010), pp. 144–146.
35. E. I. Smotrova and A. I. Nosich, "Directional light emission from a kite-shaped microcavity laser," in *Proceedings of International Conference on Transparent Optical Networks* (IEEE, 2011), paper We.A4.4.
36. E. I. Smotrova and A. I. Nosich, "Thresholds of lasing and modal patterns of a limaçon cavity analysed with Muller's integral equations," in *Proceedings of International Conference On Laser and Optical Networks Modeling* (IEEE, 2011), paper 083.
37. J. L. Tsalamengas, "Exponentially converging Nystrom methods applied to the integral-integro-differential equations of oblique scattering/hybrid mode propagation in presence of composite dielectric cylinders of arbitrary cross-section," *IEEE Trans. Antennas Propag.* **55**, 3239–3250 (2007).
38. A. N. Tikhonov and A. A. Samarskii, *Equations of Mathematical Physics* (Dover, 1990).
39. A. V. Pogorelov, *Differential Geometry* (Noordhoff, 1974).
40. Z. T. Nazarchuk, *Numerical Analysis of Wave Diffraction by Cylindrical Structures* (Naukova Dumka, 1989) (in Russian).
41. Y. V. Gandel, *Introduction to the Methods of Computation of Singular and Hyper-Singular Integrals* (Kharkiv National University, 2001) (in Russian).
42. M. Abramowitz and I. Stegun, *Handbook of Mathematical Functions* (National Bureau of Standards, 1964).
43. E. Y. Schmidt, N. V. Zorina, M. Y. Dvorko, N. I. Protsuk, K. V. Belyaeva, G. Clavier, R. Méallet-Renault, T. T. Vu, A. B. I. Mikhaleva, and B. A. Trofimov, "A general synthetic strategy for the design of new BODIPY fluorophores based on pyrroles with polycondensed aromatic and metallocene substituents," *Chem. Eur. J.* **17**, 3069–3073 (2011).
44. M. Lebental, J. S. Lauret, R. Hierle, and J. Zyss, "Highly directional stadium-shaped polymer microlasers," *Appl. Phys. Lett.* **88**, 031108 (2006).
45. I. Gozhyk, G. Clavier, R. Méallet-Renault, M. Dvorko, R. Pansu, J.-F. Audibert, A. Brosseau, C. Lafargue, V. Tsvirkun, S. Lozenko, S. Forget, S. Chénais, C. Ulysse, J. Zyss, and M. Lebental, "Polarization properties of solid-state organic lasers," *Phys. Rev. A* **86**, 043817 (2012).
46. M. V. Balaban, R. Sauleau, T. M. Benson, and A. I. Nosich, "Accurate quantification of the Purcell effect in the presence of a dielectric microdisk of nanoscale thickness," *IET Micro Nano Lett.* **6**, 393–396 (2011).